Acta Mech 219, 241–254 (2011)
DOI 10.1007/s00707-011-0451-9

S. Farhadi · S. Hosseini-Hashemi

Flutter stabilization of cantilevered plates using a bonded patch

Received: 26 May 2010 / Published online: 17 February 2011

Abstract In recent years, many researchers have studied active vibration suppression of fluttering plates using piezoelectric actuators. Lots of these researchers have focused on optimal placement of piezoelectric patches to obtain maximum controllability of the plate. Although mass and stiffness characteristics of bonded patches can alter the aeroelastic behavior of fluttering plates, few of the investigators have considered the effect of the mentioned parameters in the optimization process. This paper investigates the effect of a bonded patch on the aeroelastic behavior of cantilevered plates in supersonic flow and examines the optimal location of the patch for the best controllability performance. For mathematical simulation of the structure, linear von Karman plate theory along with first-order piston theory is employed. The results obtained through this study reveal that a bonded patch with a small mass ratio can change the system critical dynamic pressure significantly. The maximum raise of the critical dynamic pressure is acquired when the bonded patch is placed on the leading edge of the plate. A variation of the system's aerodynamic characteristics, subsequently, influences the control performance of the bonded patch and alters the optimal patch location.

1 Introduction

Recently, performance optimization of smart materials and structures has attracted many researchers. A lot of investigators focused their studies on the optimal vibration suppression of fluttering plates and panels that are ideal models for wings and membrane elements of airplanes and missiles. For this aim, one of the challenges was to obtain the optimal location of piezoelectric actuators. Therefore, lots of works were devoted to optimal placement of the bonded actuators. Most of the researchers used controllability-based optimization methods to maximize the system controllability index (for example, see Refs. [1–4]). In these methods, it is assumed that the effect of the patch's structural characteristics on the system dynamics is negligible and simply the system controllability index is investigated to obtain the best locations for actuator placement. Although, in specific patch positions, mass and stiffness characteristics of the bonded patches can considerably alter the aeroelastic behavior of fluttering plates, few researchers considered variations of system dynamics in the optimization process.

Nam et al. [5] accounted for the patch mass and stiffness effect in their optimization method by including closed loop damping ratios as design constraints in the optimization objective function. Richard and Clark [6] included patch mass and stiffness effects within their optimization routine indirectly by introducing a metric that presents a rough prediction of the effects of patch mass and stiffness contributions on the system.

S. Farhadi (✉)
Department of Mechanical Engineering, University of Kurdistan, 15175-66177, Sanandaj, Iran
E-mail: s.farhadi@uok.ac.ir

S. Hosseini-Hashemi
School of Mechanical Engineering, Iran University of Science and Technology,
16846-13114 Narmak, Tehran, Iran

In this study, the optimal location of a bonded piezoelectric patch for flutter stabilization of a cantilevered rectangular plate has been investigated via controllability and dynamic stability criterions. According to the controllability criterion, the best position for the patch placement is a position where the controllability index is maximized, i.e., a location where the maximum controllability of targeted modes is obtained. Instead, the dynamic stability criterion, which has been developed in this paper, obtains the patch locations where the flutter boundary is enhanced passively, and flow-induced vibrations can be suppressed with a small actuator effort.

For mathematical simulation of the structure, von Karman [7] plate theory is employed. Air flow pressure is modeled using first-order plate theory. This aerodynamic theory is valid for irrotational non-viscous air flows and limits our survey to the supersonic region. Kane's [8] dynamic method is utilized to obtain the governing equations of motion. Then, the critical dynamic pressure of the structure is determined with respect to the patch position.

For active control of induced vibrations, two control plans are utilized. In the first plan, just the first and the second modal states of the system are fed back, which correspond to the system fluttering modes. In the second plan, the LQR full-state feedback method is employed. With the aim of reducing the number of feed-back states and decreasing the effect of system modeling errors generated in high-frequency modes, reduced order models are used for the latter case.

Since the maximum actuation voltage is restricted by the piezo-actuator allowed voltage, this constraint must be regarded in practical controller design and patch placement methodologies. In the current analysis, for the expected vibration amplitude, the maximum required voltage is measured. This value is considered as a norm to assess the best location for actuator placement.

The obtained results show that bonding a patch with a small mass ratio to a cantilevered plate can effectively alter its critical dynamic pressure. In fact, by placing a patch on the plate, the vibration mode shapes of the plate change. Hence, aerodynamic couplings between vibrating modes are magnified or restrained.

Numerical results reveal that when merely the first and the second system modal states are used as control feedbacks, the best location for patch placement matches with those obtained by the dynamic stability criterion, i.e., the patch locations where the maximum passive stability is obtained by patch placement. This judgment is still valid when an LQR controller with low number of feedback states and a reduced model estimator are utilized. When an LQR controller with a large number of state feedbacks is employed, the best patch position is defined by maximizing the controllability index. However, utilization of such a controller will cause the designer to be faced with some mathematical and practical limitations.

While the main aim of investigators is to suppress vibrations of fluttering plates, presented results suggest that utilization of a passive–active hybrid method can present a satisfactory performance for vibration stabilization of the mentioned systems. These results suggest that there is a possibility to find actuator locations where the controllability index is not optimal; instead, the aeroelastic characteristics of the system are modified, so that the needed actuator effort reduces, and the overall control performance improves considerably.

2 Governing equations

Figure 1 shows a cantilevered plate with length a, width b, and thickness h subjected to a lateral supersonic flow of velocity V_∞. This plate is embedded with a piezoelectric patch of dimensions a_P, b_P, and h_p located at the coordinates (x_P, y_P).

According to Kane's [8] dynamic method the governing equations of motion are expressed as:

$$\mathbf{F}^* + \mathbf{F} - \mathbf{F}_{\text{ex}} = \mathbf{0} \tag{1}$$

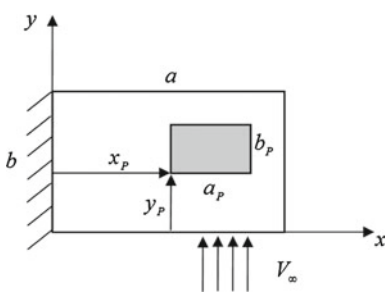

Fig. 1 A cantilevered plate with a bonded patch subjected to a lateral supersonic flow

where $\mathbf{F}^*$, $\mathbf{F}$, and $\mathbf{F}_{\text{ex}}$ are vectors of the generalized inertia forces, the generalized internal active forces, and the generalized external active forces, respectively, which are defined as follows:

$$\mathbf{F}^* = \int_V \rho \frac{\partial \mathbf{v_P}}{\partial \dot{\mathbf{q}}} \cdot \mathbf{a_P} dV, \quad \mathbf{F} = \frac{\partial U}{\partial \mathbf{q}}, \quad \mathbf{F}_{\text{ex}} = \int_V \frac{\partial \dot{w}}{\partial \dot{\mathbf{q}}} P dA \tag{2.1–3}$$

where $\mathbf{v_P}$ and $\mathbf{a_P}$ are velocity and acceleration vectors of a generic point p, respectively, $\dot{\mathbf{q}}$ stands for the time derivative of the generalized coordinates vector $\mathbf{q}$, and $\dot{w}$ is lateral velocity of the plate. In addition, P is the aerodynamic pressure, and U is the strain energy of the structure.

Velocity and acceleration vectors can be obtained as follows:

$$\mathbf{v_P} = \dot{u}_0 e_1 + \dot{v}_0 e_2 + \dot{w}_0 e_3, \quad \mathbf{a_P} = \ddot{u}_0 e_1 + \ddot{v}_0 e_2 + \ddot{w}_0 e_3 \tag{3}$$

where u_0, v_0, and w_0 denote the mid-plane deformations along the x, y, and z axes, respectively, and e_1, e_2, and e_3 stand for the corresponding unit vectors.

The strain energy of the base plate and the embedded piezoelectric patch are calculated by:

$$U_1 = \frac{1}{2} \int_V \boldsymbol{\varepsilon}^{\mathbf{T}} \boldsymbol{\sigma} dV, \tag{4.1}$$

$$U_2 = \frac{1}{2} \int_{V_P} \boldsymbol{\varepsilon}^{\mathbf{T}} \boldsymbol{\sigma} dV - \frac{1}{2} \int_{V_P} \mathbf{E}^{\mathbf{T}} \mathbf{D} dV \tag{4.2}$$

where $\boldsymbol{\sigma}$, $\boldsymbol{\varepsilon}$, $\mathbf{E}$, and $\mathbf{D}$ are vectors of stress, strain, electric field, and electric displacement components, respectively. In addition, V and V_P denote the total volume of the plate and the piezoelectric patch, respectively. The total strain energy of the structure is obtained by summing up the mentioned strain energies.

According to Hooke's law, stress and strain fields of elastic materials are related through the following equation:

$$\boldsymbol{\sigma} = \mathbf{C} \boldsymbol{\varepsilon} \tag{5}$$

where $\mathbf{C}$ is the material stiffness matrix. For plane stress problems, $\mathbf{C}$ is of the following general form:

$$\mathbf{C} = \begin{bmatrix} C_{11} & C_{12} & 0 \\ C_{12} & C_{22} & 0 \\ 0 & 0 & C_{66} \end{bmatrix}. \tag{6}$$

The constitutive equations for piezoelectric materials that relate stress, strain, and electric field vectors are as follows:

$$\boldsymbol{\sigma} = \mathbf{C}_P \boldsymbol{\varepsilon} - \mathbf{e}^{\mathbf{T}} \mathbf{E}, \tag{7.1}$$

$$\mathbf{D} = \mathbf{e} \boldsymbol{\varepsilon} + \mathbf{k} \mathbf{E}. \tag{7.2}$$

In the above equations, matrices $\mathbf{C}_P$, $\mathbf{e}$, and $\mathbf{k}$ are designated to the patch elastic coefficients, the piezoelectric coefficients, and the dielectric constants, respectively.

Assuming the electric field to be applied only in the transverse direction, the vector of electric field components can be obtained as:

$$\mathbf{E} = \frac{1}{h_p} \bar{\mathbf{E}} V_3, \quad \bar{\mathbf{E}} = \begin{bmatrix} 0 & 0 & -1 \end{bmatrix}^T \tag{7.3}$$

where V_3 represents the applied voltage to the piezoelectric patch.

According to von Karman plate theory, linear components of the strain field are obtained through the following equations:

$$\begin{aligned} \varepsilon_{\text{xx}} &= \frac{\partial u_0}{\partial x} - z \frac{\partial^2 w_0}{\partial x^2}, \\ \varepsilon_{\text{yy}} &= \frac{\partial v_0}{\partial y} - z \frac{\partial^2 w_0}{\partial y^2}, \\ \varepsilon_{\text{xy}} &= \frac{\partial u_0}{\partial y} + \frac{\partial v_0}{\partial x} - 2z \frac{\partial^2 w_0}{\partial x \partial y}, \end{aligned} \tag{8}$$

and the strain vector is formed as below:

$$\boldsymbol{\varepsilon} = \begin{bmatrix} \varepsilon_{xx} & \varepsilon_{yy} & \varepsilon_{xy} \end{bmatrix}^T. \tag{9}$$

First-order piston theory is employed to obtain the aerodynamic pressure. This theory is used for steady flows with Mach number higher than 1.6 and determines the air dynamic pressure as follows [10]:

$$P = -\frac{\rho_a V_\infty^2}{\beta}\left(\frac{\partial w}{\partial y} + \frac{1}{V_\infty}\left(\frac{M_\infty^2 - 2}{M_\infty^2 - 1}\right)\frac{\partial w}{\partial t}\right). \tag{10}$$

In the above equation, ρ_a and M_∞ denote the air density and free stream Mach number, respectively, and β is a dimensionless number defined as $\beta = \sqrt{M_\infty^2 - 1}$.

Using the Ritz method, the displacement field components can be approximated as follows:

$$\begin{aligned} u_0 &= \sum_{j=1}^{N_1}\sum_{i=1}^{M_1} a_{i+(j-1)M_1} G_1(x, y)\Phi_i(x)\Psi_j(y), \\ v_0 &= \sum_{j=1}^{N_2}\sum_{i=1}^{M_2} b_{i+(j-1)M_2} G_2(x, y)\Phi_i(x)\Psi_j(y), \\ w_0 &= \sum_{j=1}^{N_3}\sum_{i=1}^{M_3} c_{i+(j-1)M_3} G_3(x, y)\Phi_i(x)\Psi_j(y) \end{aligned} \tag{11}$$

where $a_{i+(j-1)M_1}$, $b_{i+(j-1)M_2}$, and $c_{i+(j-1)M_3}$ are time-dependent coefficients, $\Phi_i(x)$ and $\Psi_j(y)$ are arbitrary functions, $G_i\ (x, y)$ are manipulator functions satisfying the geometrical boundary conditions, and N_1, N_2, N_3 and M_1, M_2, M_3 are the number of terms used in the approximation functions in x and y direction, respectively. For a plate cantilevered in the edge $x = 0$, the manipulator functions are obtained as $G_i\ (x, y) = x,\ i = 1, 2, 3$. For convenience, the above-assumed displacement functions are expressed in matrix form as:

$$\mathbf{d} = \begin{Bmatrix} u_0 \\ v_0 \\ w_0 \end{Bmatrix} = \mathbf{Nq}, \quad \mathbf{q} = \begin{Bmatrix} \mathbf{a} \\ \mathbf{b} \\ \mathbf{c} \end{Bmatrix} \tag{12}$$

where $\mathbf{N}$ is the matrix of shape functions, and $\mathbf{q}$ is the generalized coordinates vector. Moreover, $\mathbf{a}$, $\mathbf{b}$, and $\mathbf{c}$ are vectors made of the corresponding time-dependent coefficients reported in Eq. (10).

Introducing the following operator matrices:

$$\mathbf{H_1} = \begin{bmatrix} 1\ 0\ 0 \end{bmatrix}, \quad \mathbf{H_2} = \begin{bmatrix} 0\ 1\ 0 \end{bmatrix}, \quad \mathbf{H_3} = \begin{bmatrix} 0\ 0\ 1 \end{bmatrix}, \quad \mathbf{H_4} = \begin{bmatrix} \frac{\partial}{\partial y}\ 0\ 0 \end{bmatrix}, \tag{13}$$

$$\mathbf{L_i} = \mathbf{H_i N}, \quad \mathbf{S_j} = \mathbf{B_j N}, \tag{14}$$

$$\mathbf{B_1} = \begin{bmatrix} \frac{\partial}{\partial x} & 0 & -z\frac{\partial^2}{\partial x^2} \\ 0 & \frac{\partial}{\partial y} & -z\frac{\partial^2}{\partial y^2} \\ \frac{\partial}{\partial y} & \frac{\partial}{\partial x} & -2z\frac{\partial^2}{\partial x \partial y} \end{bmatrix}, \quad \mathbf{B_2} = \begin{bmatrix} 0 & 0 & \frac{\partial}{\partial x} \\ 0 & 0 & \frac{\partial}{\partial y} \\ 0 & 0 & \frac{\partial}{\partial y} \end{bmatrix} \tag{15}$$

and substituting Eqs. (3–12) into Eq. (2), the generalized equations of motion are derived as follows:

$$\mathbf{M}\ddot{\mathbf{q}} + \mathbf{C_A}\dot{\mathbf{q}} + (\mathbf{K} + \mathbf{K_A})\,\mathbf{q} = \mathbf{F}V_3 \tag{16}$$

where $\mathbf{M}$, $\mathbf{K}$, $\mathbf{C_A}$, and $\mathbf{K_A}$ are the mass, the stiffness, the aerodynamic damping, and the aerodynamic stiffness matrices, respectively, and $\mathbf{F}$ is the piezoelectric patch actuating vector. These matrices and vectors are

introduced below:

$$\mathbf{M} = \rho \int\limits_{V+V_P} \left(\mathbf{L_1^T L_1} + \mathbf{L_2^T L_2} + \mathbf{L_3^T L_3}\right) dV, \tag{17}$$

$$\mathbf{K} = \int\limits_{V} \mathbf{S_1^T C S_1} dV + \int\limits_{V_P} \mathbf{S_1^T C}_P \mathbf{S_1} dV, \tag{18}$$

$$\mathbf{C_A} = \frac{\rho_a \mathrm{V}_\infty}{\beta} \left(\frac{M_\infty^2 - 2}{M_\infty^2 - 1}\right) \int\limits_{A} \mathbf{L_3^T L_3} dA, \tag{19}$$

$$\mathbf{K_A} = \frac{\rho_a \mathrm{V}_\infty^2}{\beta} \int\limits_{A} \mathbf{L_3^T L_4} dA, \tag{20}$$

$$\mathbf{F} = \frac{1}{h_P} \int\limits_{V_P} \mathbf{S_1^T e^T E} dV. \tag{21}$$

In Eqs. (17–21), the introduced integrals are calculated over the total volume including the volume of the plate and the patch.

3 Critical dynamic pressure

Omitting the piezoelectric actuating vector from (16), the following equation is obtained:

$$\mathbf{M}\ddot{\mathbf{q}} + \mathbf{C_A}\dot{\mathbf{q}} + (\mathbf{K} + \mathbf{K_A})\,\mathbf{q} = \mathbf{0}. \tag{22}$$

Assuming the generalized coordinates vector to be harmonic ($\mathbf{q} = \bar{\mathbf{q}} e^{i\omega t}$), this equation reduces to a conventional eigenvalue problem:

$$\left(\mathbf{M}\alpha^2 - \mathbf{C_A}\alpha + \mathbf{K} + \mathbf{K_A}\right)\bar{\mathbf{q}} = \mathbf{0} \tag{23}$$

where the corresponding eigenvalues depend on the flow characteristics and in general form are complex values, as follows:

$$\alpha = \eta + i\omega. \tag{24}$$

In the above equation, ω specifies the vibration frequency and η shows the damping rate.

In Aeroelasticity field, the system behavior is commonly discussed in terms of the dimensionless dynamic pressure λ, which is

$$\lambda = \frac{\rho_a V_\infty^2 a^3}{D}, \quad D = \frac{C_{11} h^3}{12} \tag{25}$$

where D and h stand for flexural rigidity of the plate and the plate thickness, respectively, and C_{11} indicates the first element of the plate stiffness matrix.

Solving the characteristic Eq. (23) for different values of dimensionless dynamic pressures, it is observed that for small values of λ the plate damping rate η is negative, which indicates that the plate vibrations decay gradually and the system is stable. On the other hand, the damping rate value μ becomes positive, and plate oscillations turn into the unstable zone when the dynamic pressure goes beyond a critical value. This value is commonly referred as critical dynamic pressure (λ_{cr}). In practice, the existence of nonlinear stiffness terms in the governing equation limits the amplitude of vibration to a bounded value.

Table 1 Critical dynamic pressure predicted by the current analysis for different order of approximation series and comparison with the exact solution [9]

$N \times M$	4×4	5×5	6×6	7×7	8×8	Exact [9]	Error percent
λ_{cr}/β	627.9	439.7	520.8	517.6	518.0	512.6	1.05

Table 2 Material properties of the base plate and the bonded patch

	C_{11} (GPa)	C_{12} (GPa)	C_{22} (GPa)	C_{66} (GPa)	$\rho\ (\mathrm{kg/m^3})$
Aluminum	76.92	23.08	76.92	26.92	2,700
PZT5H [11]	130.6	85.66	135.8	22.99	7,740

4 Effect of the patch position on the critical dynamic pressure

In the present work, power series are used as arbitrary functions ($\Phi_i(x) = x^{i-1}$ and $\Psi_j(y) = y^{j-1}$). For convenience, the approximation series in different directions are taken of the same order ($M_1 = M_2 = M_3 = M$ and $N_1 = N_2 = N_3 = N$). Presented results are obtained in terms of the following dimensionless values:

$$\eta = \frac{a}{b}, \quad \delta = \frac{h}{a}, \quad \bar{a} = \frac{a_p}{a}, \quad \bar{b} = \frac{b_p}{a}, \quad \bar{h} = \frac{h_p}{h}, \quad X = \frac{x_P}{a}, \quad Y = \frac{y_P}{b}, \quad \mu = \frac{b\rho_a}{h\rho}. \tag{26}$$

Here, the characteristic matrices $\mathbf{M}$, $\mathbf{C_A}$, $\mathbf{K_A}$, and $\mathbf{K}$ are calculated through exact analytical integrations using Mathematica software.

Table 1 presents a convergence study for the critical dynamic pressure of a simply supported square plate and compares the calculated value with the exact solution of the problem [9]. This Table shows that with polynomial approximation series of order $N \times M = 8 \times 8$, the calculated critical dynamic pressure converges to the exact solution with an adequate precision.

In order to study the patch placement effect on the critical dynamic pressure, a cantilevered plate with the following dimensional values is considered:

$$a = 0.4\,\mathrm{m}, \quad \delta = 4/3, \quad \eta = 0.01. \tag{27}$$

A rectangular patch with the following dimensions is bonded to the plate:

$$\bar{a} = 1/4, \quad \bar{b} = 5/30, \quad \bar{h} = 1/4. \tag{28}$$

In this paper, the free-stream Mach number is set to $M_\infty = 2$, and the air–panel mass ratio is considered as $\mu = 0.1$.

An aluminum base plate is considered ($E = 70$ GPa and $v = 0.3$), and two materials are considered for the embedded patch, namely aluminum and PZT5H. The employed material coefficients are reported in Table 2 [11]. The critical dynamic pressure of the base plate is $\lambda_{cr} = 143.8$.

Bonding a patch to the cantilever plate modifies the mass and stiffness matrices by some values, depending on the patch position, which in turn changes the critical dynamic pressure. Although the mode shapes of the base plate are symmetric with respect to the plate central axis, the effect of patch placement on the critical dynamic pressure is not symmetric. This asymmetry is caused by fluid flow that is unidirectional and asymmetric. Figures 2a, b exhibit variations of the critical dynamic pressure versus patch position for an aluminum cantilevered plate with an aluminum patch and with a piezoelectric patch, respectively. According to the patch dimensions (Eq. (28)) and patch density (Table 2), the patch to plate mass ratio is .01 for the aluminum patch and is 0.03 for the piezoelectric patch. However, from Fig. 2a, it is observed that the placement of these patches can increase the critical dynamic pressure of the base plate extensively. Calculations show that for the case with the aluminum patch the maximum value of the critical dynamic pressure is about 32% larger than the base value, and for the case of a piezoelectric patch, this value is about 50% larger than the base one. It means that bounding a patch with rather small mass ratio to a cantilevered plate alters its dynamic characteristics significantly. Figure 2b shows that the maximum increment of the critical dynamic pressure is achieved when the patch is bonded at the plate free corner on the leading edge (i.e., $(X, Y) = (0.75,0)$).

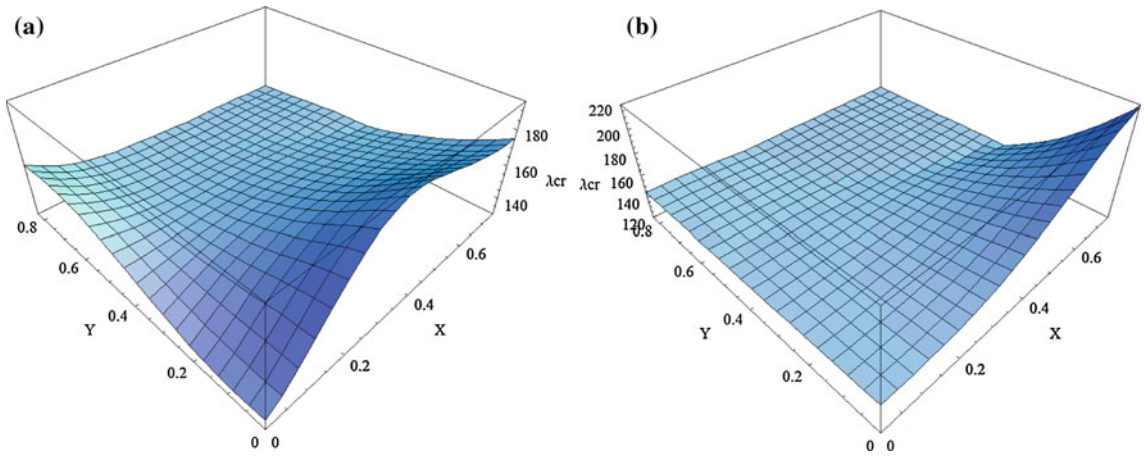

Fig. 2 Variations of critical dynamic pressure versus patch location; **a** with an aluminum patch, **b** with a PZT5H patch

5 Optimal placement of the bonded patch

Transferring the equations of motion to the state space, the following equation is obtained:

$$\dot{\mathbf{Z}} = \mathbf{A}\mathbf{Z} + \mathbf{B}V_3 \tag{29}$$

where

$$\mathbf{Z} = \begin{Bmatrix} \mathbf{q} \\ \dot{\mathbf{q}} \end{Bmatrix}, \quad \mathbf{A} = -\begin{bmatrix} \mathbf{I} & \mathbf{0} \\ \mathbf{0} & \mathbf{M} \end{bmatrix}^{-1} \cdot \begin{bmatrix} \mathbf{0} & -\mathbf{I} \\ \mathbf{K} + \mathbf{K_A} & \mathbf{C_A} \end{bmatrix}, \quad \mathbf{B} = \begin{bmatrix} \mathbf{I} & \mathbf{0} \\ \mathbf{0} & \mathbf{M} \end{bmatrix}^{-1} \cdot \begin{Bmatrix} 0 \\ \mathbf{F} \end{Bmatrix}. \tag{30}$$

Here, in order to obtain the optimal location of a single piezoelectric patch for multi-mode vibration control of the plate, we use the modal controllability theorem [12]. Based on this theory, the degree of controllability of each arbitrary mode can be defined by the angle between the corresponding mode eigen-vector and the actuation vector **B**:

$$C_i = \cos(\theta_i) = \frac{\boldsymbol{\psi}_\mathbf{i}^\mathbf{T}.\mathbf{B}}{\|\boldsymbol{\psi}_i\| \,.\, \|\mathbf{B}\|} \tag{31}$$

where $\boldsymbol{\psi}_\mathbf{i}$ defines the left eigen-vector corresponding to the ith vibration mode, and C_i stands for the controllability degree of that mode.

It is worth mentioning that aerodynamic couplings between different vibration modes result in complex conjugate eigen-vectors. Hence, the controllability degrees obtained by Eq. (31) consist of real and imaginary parts. In order to have a real number, in this paper, absolute values of controllability degrees are used.

A disadvantage of the modal controllability theorem is that this theory does not account for variations of system aerodynamic characteristics, directly, which are introduced by the patch location.

6 Dynamic stabilization criterion

In order to assess the effect of the patch position on the aerodynamic instability boundary, a criterion is developed in the sequel. Since for the case of cantilevered plates subjected to lateral air flow the aerodynamic instability results from aerodynamic couplings between the first and the second vibration modes, we develop the dynamic stability criterion based on the modal damping ratios corresponding to the mentioned modes.

A typical plot of eigenvalue real and imaginary parts corresponding to the plate coupled modes versus air dynamic pressure is given in Fig. 3. In this figure, η and ω are designated to the real part and imaginary parts of the system eigenvalues, respectively. Figure 3a shows that in rather small values of the dynamic pressure the real parts of eigenvalues are negative identical values. These two values then exhibit a rapid divergence as the dynamic pressure increases, and beyond a critical value, one of them turns into positive and vibration instability. As shown in Fig. 3b, a frequency locking is observed in the critical dynamic pressure. Modal damping

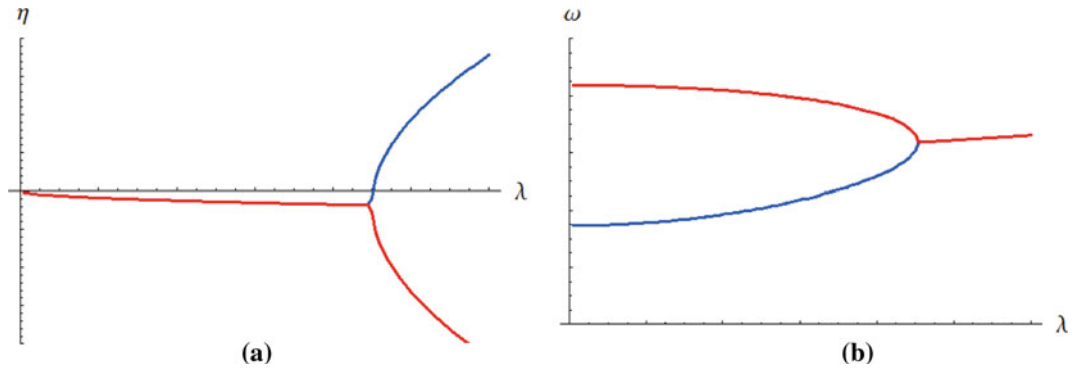

Fig. 3 Eigenvalue real and imaginary parts of plate coupled modes versus air dynamic pressure; **a** real part, **b** imaginary part

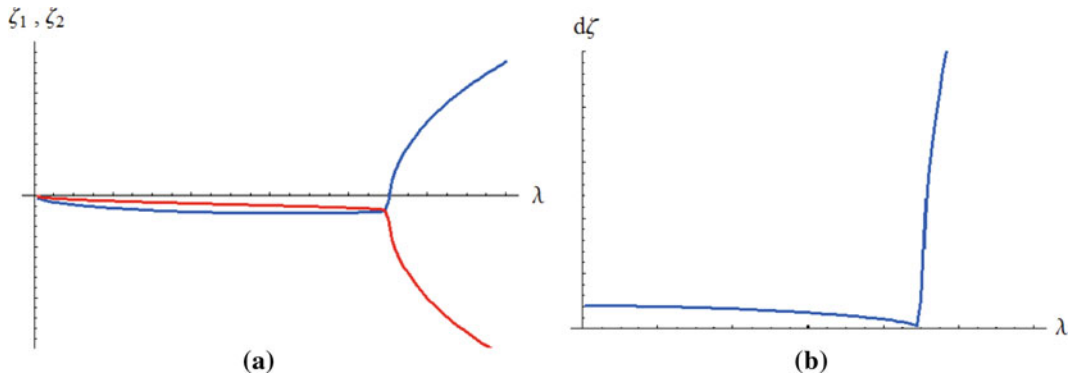

Fig. 4 Modal damping ratios of the coupled modes and the dynamic stability criterion versus the dynamic pressure; **a** Modal damping ratios, **b** dynamic stability criterion

ratios of the mentioned coupled modes are illustrated in Fig. 4a. From this figure, one can see that by increasing the dynamic pressure, monotonically, the modal damping ratios increase first and the dynamic stability improves. Then, the damping loci converge to an identical value, and finally a rapid divergence arises, and one of the branches enters the instability region. In the dynamic pressures close to the value corresponding to the divergence point, the maximum values of damping ratios are acquired, and maximum stability is obtained for the studied modes. Hence, it is reasonable to consider the mentioned divergence point as a metric to assess the dynamic stability condition. In this paper, the following criterion is introduced to assess the stability condition:

$$d\xi = \left| \frac{\xi_1 - \xi_2}{\xi_1 + \xi_2} \right| \tag{32}$$

where ξ_1 and ξ_2 are modal damping ratios corresponding to the first and the second vibration modes, respectively, and are defined through the following equation:

$$\xi = \sqrt{\left(\frac{\eta}{\omega}\right)^2 \Big/ \left(1 + \left(\frac{\eta}{\omega}\right)^2\right)} Sign(\eta). \tag{33}$$

Placing the piezoelectric patch in positions where the dynamic stability criterion Eq. (32) is minimized, one can obtain the best patch location for passive stabilization of the fluttering plate. A typical plot of the dynamic stability criterion versus the dynamic pressure is demonstrated in Fig. 4b.

7 State vector feedback control

With the aim of stabilizing the plate vibrations actively, a state vector feedback method is employed. In this method, the patch applied voltage is considered as a gain of the system modal states vector. For this purpose, the equations of motion are transferred to the modal space with the following transformation:

$$\mathbf{Z} = \boldsymbol{\varphi}\mathbf{x} \tag{34}$$

where $\boldsymbol{\varphi}$ denotes the system's right eigenvectors matrix. Employing the above transformation to Eq. (29) yields:

$$\dot{\mathbf{X}} = \bar{\mathbf{A}}\mathbf{X} + \bar{\mathbf{B}}V_3 \tag{35}$$

where $\bar{\mathbf{A}}$ and $\bar{\mathbf{B}}$ are defined as:

$$\begin{aligned} \bar{\mathbf{A}} &= \boldsymbol{\varphi}^{-1}\mathbf{A}\boldsymbol{\varphi}, \\ \bar{\mathbf{B}} &= \boldsymbol{\varphi}^{-1}\mathbf{B}. \end{aligned} \tag{36}$$

Finally, the applied voltage V_3 is introduced as follows:

$$V_3 = -\mathbf{K_V}\mathbf{X}. \tag{37}$$

In the above equation, $\mathbf{K_V}$ is a single row matrix, which components define the gains of system state feedbacks.

In Eq. (37), two methods are used to define modal feedback gains. In the first method, only the first and the second modal states are feedback:

$$\mathbf{K_V} = k_v \begin{bmatrix} 1 & 1 & 0 & 0 \cdots 0 \end{bmatrix}. \tag{38}$$

In the above equation, k_v is defined such that the critical dynamic pressure shifts to an aimed value.

In the second method, the LQR method is employed. This method obtains $\mathbf{K_V}$ through minimization of the following scalar performance index:

$$J = \int_0^t \mathbf{X^T Q X} + V_3^T \mathbf{R} V_3 \, dt \tag{39}$$

where $\mathbf{Q}$ and $\mathbf{R}$ are symmetric gaining matrices, and for single input systems, $\mathbf{R}$ is a scalar value. In the current study, we have taken all components of the gaining matrix $\mathbf{Q}$ to be zero except the diagonal values corresponding to the first and the second vibration modes that are taken equal to identical number $\bar{Q}$.

Subsequently, for the expected vibration amplitude, the maximum required voltage is measured. This value is considered as a norm to assess the best location for actuator placement.

From Eq. (37), one can see that the required applied voltage is a function of the system vibration mode and amplitude. Thus, it is crucial to have a reasonable assumption for the system initial conditions to measure the maximum control voltage required to suppress the flow-induced vibrations. According to the experimental data published in the literature [13], in the dynamic pressures lower than the critical value, random oscillations of the panel are observed with dominant frequency components close to the lower panel natural frequencies, and the maximum amplitude vibration is a small fraction of the panel thickness. As the flutter boundary is exceeded, the amplitude of vibrations increases to the order of the plate thickness when the dynamic pressure increases from 25 to 100% beyond the critical value. In the current study, for the definition of initial conditions, we assume the plate to be deflected in its first vibration mode shape so that the lateral displacement in dimensionless coordinates $(X, Y) = (1, 3/4)$ is $w_0/h = 0.5$.

Contour plots corresponding to the different optimization methods are collected in Table 3. The contour plots are presented with respect to the patch dimensionless coordinates ($X = x_p/a$ and $Y = y_p/b$) for different base dynamic pressures (λ_b). In the presented plots, the black and white colors indicate the minimum and the maximum values in the range, respectively. The dimensionless coordinates corresponding to the optimal locations defined by the previous analysis are presented in Table 4. According to this table, in the dynamic pressures lower than the critical value ($\lambda_{cr} = 143.8$), the optimal locations defined by the dynamic stability criterion match with the locations where the modal damping ratio of the second vibration mode is minimized. However, when the critical dynamic pressure is exceeded, these locations match with those where the modal damping ratio of the first vibration mode is minimized. It is worth mentioning that in dynamic pressures lower than the critical value the modal damping ratio of the first vibration mode is smaller than the one corresponding to the second vibration mode (regarding the negative sign of the values). However, when the dynamic pressure goes beyond the critical value, the situation becomes reversed. Since the dynamic stability criterion seeks for the locations where the minimum difference between normal damping ratios exists, it determines the locations where the modal damping ratio of less stable mode is minimized.

Table 3 Contour plots corresponding to the different patch placement criterions versus dimensionless patch position

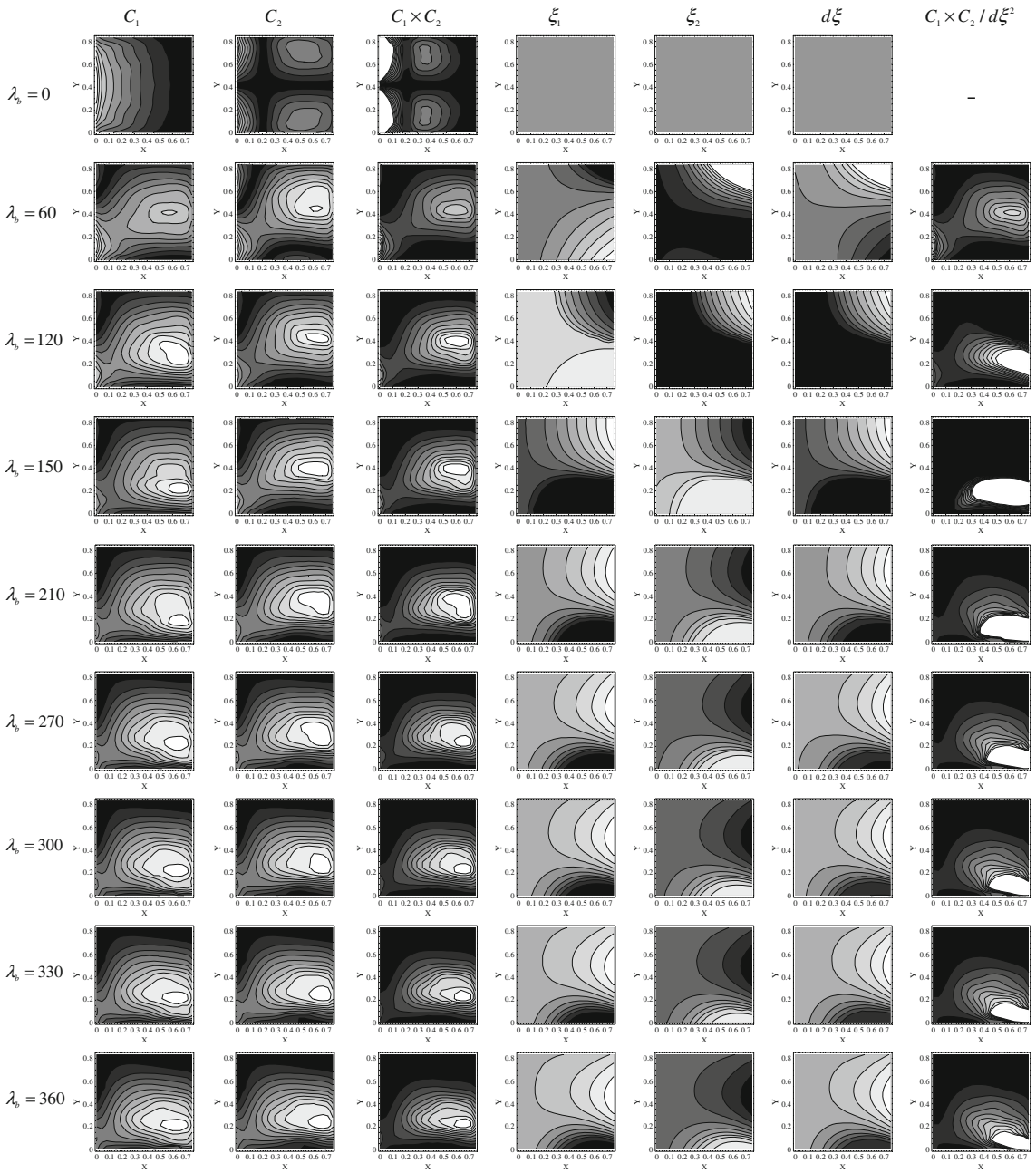

The calculations are performed for different values of flow dynamic pressure (λ_b). The black and white colors indicate the minimum and the maximum values, respectively

The maximum voltage required to stabilize the flow-induced vibrations in dynamic pressures $\lambda = 210$ and $\lambda = 290$ is presented in Tables 5 and 6, respectively. The presented values are obtained by feeding back the modal state corresponding to the first vibration mode and placing the piezoelectric patch in the optimal locations defined in the previous analysis. From Tables 5 and 6, it is obvious that in some patch locations the vibration stabilization is provided passively. Moreover, in some patch locations, it is essentially impossible to stabilize the induced vibrations.

Table 4 Dimensionless optimal locations defined by different patch placement criteria

	$Max(C_1)$	$Max(C_2)$	$Max(C_1 \times C_2)$	$Min(\xi_1)$	$Min(\xi_2)$	$Min(d\xi)$	$Max\left(\frac{C_1 \times C_2}{d\xi^2}\right)$
$\lambda_b = 0$	(0,5/12)	(0,1/8)	(0,1/8)	–	–	–	–
$\lambda_b = 60$	(0,1/8)	(0,1/12)	(0,1/8)	(3/4,5/6)	(21/40,1/4)	(3/4,0)	(0,1/8)
$\lambda_b = 120$	(27/40,1/4)	(51/80,5/12)	(3/5,5/12)	(3/4,5/6)	(3/8,5/24)	(3/4,0)	(57/80,5/24)
$\lambda_b = 150$	(27/40,5/24)	(3/5,5/12)	(3/5,3/8)	(33/80,5/24)	(3/4,3/4)	(51/80,1/8)	(51/80,5/24)
$\lambda_b = 210$	(51/80,1/6)	(51/80,3/8)	(3/5,3/8)	(51/80,1/24)	(3/4,7/12)	(27/40,0)	(27/40,1/8)
$\lambda_b = 270$	(51/80,5/24)	(27/40,1/4)	(27/40,1/4)	(57/80,0)	(3/4,13/24)	(57/80,0)	(57/80,1/12)
$\lambda_b = 300$	(51/80,5/24)	(27/40,1/4)	(27/40,1/4)	(57/80,0)	(3/4,1/2)	(57/80,0)	(27/40,1/12)
$\lambda_b = 330$	(51/80,5/24)	(27/40,1/4)	(27/40,5/24)	(57/80,0)	(3/4,11/24)	(57/80,0)	(27/40,1/12)
$\lambda_b = 360$	(51/80,5/24)	(27/40,1/4)	(27/40,5/24)	(27/40,0)	(3/4,11/24)	(27/40,0)	(57/80,1/24)
$\lambda_b = 390$	(51/80,5/24)	(27/40,5/24)	(51/80,5/24)	(51/80,0)	(3/4,1/2)	(51/80,0)	(57/80,1/24)

The calculations are performed for different values of the flow dynamic pressure (λ_b)

Table 5 Maximum actuator voltage required to stabilize the flow-induced vibrations in the dynamic pressure $\lambda = 210$ through feeding back the first modal state of the system

	$Max(C_1)$	$Max(C_2)$	$Max(C_1 \times C_2)$	$Min(\xi_1)$	$Min(\xi_2)$	$Min(d\xi)$	$Max\left(\frac{C_1 \times C_2}{d\xi^2}\right)$
$\lambda_b = 0$	1,13,100	20,056	20,056	–	–	–	–
$\lambda_b = 60$	20,056	17,627	20,056	1,513,300	4,913	Stable	20,056
$\lambda_b = 120$	5,216	16,786	15,053	1,513,300	5,453	Stable	3,670
$\lambda_b = 150$	3,444	15,053	11,456	4,930	Buckle	1,226	180
$\lambda_b = 210$	2,177	12,494	11,456	180	164,424	Stable	1072
$\lambda_b = 270$	3,403	5,216	5,216	Stable	82,510	Stable	301
$\lambda_b = 300$	3,403	5,216	5,216	Stable	51,060	Stable	401
$\lambda_b = 330$	3,403	5,216	3,444	Stable	34,521	Stable	401
$\lambda_b = 360$	3,403	5,216	3,444	Stable	34,521	Stable	51

The data are organized according to the optimal locations defined by different placement criteria for different base dynamic pressures λ_b

Table 6 Maximum actuator voltage required to stabilize the flow-induced vibrations in the dynamic pressure $\lambda = 290$ through feeding back the first modal state of the system

	$Max(C_1)$	$Max(C_2)$	$Max(C_1 \times C_2)$	$Min(\xi_1)$	$Min(\xi_2)$	$Min(d\xi)$	$Max\left(\frac{C_1 \times C_2}{d\xi^2}\right)$
$\lambda_b = 0$	Buckle	1,36,500	1,36,500	–	–	–	–
$\lambda_b = 60$	1,36,500	1,14,270	1,36,500	Buckle	9,707	1,457	1,36,500
$\lambda_b = 120$	10,491	25, 590	24, 583	Buckle	9,746	1,457	8,791
$\lambda_b = 150$	8,307	24, 583	19, 152	9,117	Buckle	4,838	7,995
$\lambda_b = 210$	6,242	20, 160	19, 152	2,774	98,658	1,852	4,863
$\lambda_b = 270$	7,995	10, 491	10, 491	1,635	67,396	1,635	3,624
$\lambda_b = 300$	7,995	10, 491	10, 491	1,635	49,126	1,635	3,595
$\lambda_b = 330$	7,995	10, 491	8, 307	1,635	37,555	1,635	3,595
$\lambda_b = 360$	7,995	10, 491	8, 307	1,852	37,555	1,852	2,438

The data are organized according to the optimal locations defined by different placement criteria for different base dynamic pressures λ_b

Tables 5 and 6 clearly show that the dynamic stability criterion yields the best locations for suppressing flow-induced vibrations if the first modal state is fed back. Similar results can be achieved for the case where only the second modal state is fed back. Here, for brevity, the corresponding results are not included.

In the sequel, an LQR controller is used to suppress the flow-induced vibrations. The LQR method is based on feeding back all states of the system. The system states should be measured directly or be estimated through the state estimation techniques. When the system states are not obtained precisely, the fed-back states can destabilize the system dynamics. It is well known that when the Ritz finite series approximation method is employed to approximate the system displacement field, nearly half of the vibration modes can be defined with an acceptable precision. These vibration modes lay in the low-frequency spectrum. Therefore, in practical usages, to reduce the number of estimated and fed-back system states, a reduced model of the system is utilized in the LQR control method. In the proceeding analysis, a reduced model with 5 vibration modes (10 modal states) and a reduced model with 10 vibration modes (20 modal states) are used.

Table 7 Maximum actuator voltage required for an LQR controller to stabilize the flow-induced vibrations

	Pos1 (51/80,5/24)	Pos2 (27/40,1/4)	Pos3 (57/80,0)	Pos4 (27/40,0)	Pos5 (51/80,0)	Pos6 (3/4,11/24)	Pos7 (3/4,1/2)
$\lambda = 290$	2,468	2,298	1,700	2,036	1,897	2,559	2,655
$\lambda = 360$	4,128	3,768	5,265	3,964	3,314	3,928	4,049
$\lambda = 390$	4,877	4,435	7,246	5,252	4,248	4,546	4,677
$\lambda = 490$	7,498	6,780	15,695	10,388	7,738	6,714	6,885

A reduced model with 5 vibration modes is considered. The actuator is placed in different positions, and the calculations are performed for different values of the air dynamic pressure

Table 8 Maximum actuator voltage required for an LQR controller to stabilize the flow-induced vibrations

	Pos1 (51/80,5/24)	Pos2 (27/40,1/4)	Pos3 (57/80,0)	Pos4 (27/40,0)	Pos5 (51/80,0)	Pos6 (3/4,11/24)	Pos7 (3/4,1/2)
$\lambda = 290$	213	249	1,079	2,350	2,812	16	83
$\lambda = 360$	419	478	976	1,722	2,270	30	186
$\lambda = 390$	522	595	986	1,686	2,191	39	248
$\lambda = 490$	926	1,049	1,072	1,749	2,193	102	573

A reduced model with 10 vibration modes is considered. The actuator is placed in different positions, and the calculations are performed for different values of the air dynamic pressure

For this purpose, first, plate vibration mode shapes are obtained by omitting aerodynamic damping and stiffness matrices from Eq. (22). Then, the plate deformation field is approximated using limited numbers of out-of-plane mode shapes, as follows:

$$\begin{Bmatrix} u_0 \\ v_0 \\ w_0 \end{Bmatrix} = r_1 \mathbf{N}\boldsymbol{\varphi_1} + r_2 \mathbf{N}\boldsymbol{\varphi_2} + \cdots + r_n \mathbf{N}\boldsymbol{\varphi_n} = \bar{\mathbf{N}}\mathbf{r} \tag{40}$$

where $r_1, r_2, \ldots, r_n$ are time-dependent coefficients, $\boldsymbol{\varphi_1}, \boldsymbol{\varphi_2}, \ldots, \boldsymbol{\varphi_n}$ are eigenvectors corresponding to the selected mode shapes, $\mathbf{N}$ is the matrix of mode shapes corresponding to the original system, $\bar{\mathbf{N}}$ is the matrix of mode shapes corresponding to the reduced model, and $\mathbf{r}$ stands for the vector of generalized coordinates of the reduced model.

Using the new approximation series presented in the above equation, the governing equations of the reduced model are obtained as follows:

$$\bar{\mathbf{M}}\ddot{\mathbf{r}} + \bar{\mathbf{C}}_\mathbf{A}\dot{\mathbf{r}} + \left(\bar{\mathbf{K}} + \bar{\mathbf{K}}_\mathbf{A}\right)\mathbf{r} = \bar{\mathbf{F}}. \tag{41}$$

The characteristic matrices $\bar{\mathbf{M}}$, $\bar{\mathbf{C}}_\mathbf{A}$, $\bar{\mathbf{K}}$, $\bar{\mathbf{K}}_\mathbf{A}$, and the actuation vector $\bar{\mathbf{F}}$ introduced in (41) are computed by replacing $\mathbf{N}$ with $\bar{\mathbf{N}}$ in Eq. (14).

In order to transfer the above equation to modal space, Eq. (34) is modified with the following transformation equation:

$$\mathbf{Z} = \begin{Bmatrix} \mathbf{r} \\ \dot{\mathbf{r}} \end{Bmatrix}, \mathbf{A} = -\begin{bmatrix} \mathbf{I} & \mathbf{0} \\ \mathbf{0} & \bar{\mathbf{M}} \end{bmatrix}^{-1} \cdot \begin{bmatrix} \mathbf{0} & -\mathbf{I} \\ \bar{\mathbf{K}} + \bar{\mathbf{K}}_\mathbf{A} & \bar{\mathbf{C}}_\mathbf{A} \end{bmatrix}, \mathbf{B} = \begin{bmatrix} \mathbf{I} & \mathbf{0} \\ \mathbf{0} & \bar{\mathbf{M}} \end{bmatrix}^{-1} \cdot \begin{Bmatrix} 0 \\ \bar{\mathbf{F}} \end{Bmatrix}. \tag{42}$$

MATLAB control toolbox is utilized to determine the LQR feedback gains. In order to facilitate the comparison between the obtained results for different patch locations, identical $\mathbf{Q}$ and $\mathbf{R}$ matrices are used for all cases. However, it is evident that better control performance can be acquired if suitable gaining matrices are obtained for each studied case.

Tables 7 and 8 present the maximum control voltage required to suppress the plate flutter with respect to the flow dynamic pressure for a 5 DOF and a 10 DOF model, respectively.

In Tables 7 and 8, seven patch locations are studied, which are as follows:

- Pos.1 corresponds to a patch location where the maximum controllability of the plate first vibration mode is acquired for dynamic pressures between $\lambda_b = 270$ and $\lambda_b = 360$.
- Pos. 2 is the optimal location to control the plate second modal state in dynamic pressures between $\lambda_b = 270$ and $\lambda_b = 360$. This location also possesses the maximum multi-mode controllability over the first and the second vibration modes in dynamic pressures between $\lambda_b = 270$ and $\lambda_b = 300$.

- Pos. 3 corresponds to a patch location where the minimum modal damping ratio for the first modal state and the minimum dynamic stability criterion are obtained for dynamic pressures between $\lambda_b = 270$ and $\lambda_b = 330$.
- Pos. 4 defines a patch location where the minimum modal damping ratio for the first modal state and the minimum dynamic stability criterion are obtained for a dynamic pressure $\lambda_b = 360$.
- Pos. 5 determines a patch location where the minimum modal damping ratio for the first modal state and the minimum dynamic stability criterion are achieved for a dynamic pressure $\lambda_b = 390$.
- Pos. 6 corresponds to a patch location where the minimum modal damping ratio for the second modal state is obtained for the dynamic pressures $\lambda_b = 270$ and $\lambda_b = 330$.
- Pos. 7 corresponds to a patch location where the minimum modal damping ratio for the second modal state is obtained for the dynamic pressures $\lambda_b = 300$ and $\lambda_b = 390$.

Table 7 shows that for the case of a 5 DOF model the best patch location is obtained by the dynamic stability criterion ($Min(d\xi)$). In fact, the dynamic stability criterion defines positions where the instability source (i.e., aerodynamic coupling between fluttering modes) is weakened passively to a significant level. Thus, in the corresponding locations, the LQR controller can suppress the flow-induced vibrations with a small control effort.

Comparing Tables 7 and 8, it is observed that feeding back more state variables, in theory, facilitates vibration stabilization with lower values of the control voltage. Table 8 shows that the optimal location for the actuator placement does not match with the locations defined by the maximum controllability criterion ($Max(C_1 \times C_2)$) and maximum stability criterion ($Min(d\xi)$). For example, in the locations where stability is minimized (the locations obtained with $Min(\xi_1)$ and $Min(\xi_2)$ for the dynamic pressures lower than the critical value and higher than the critical value, respectively), control performance is better than the locations obtained by the maximum controllability and the maximum stability criteria. Actually, strong aerodynamic couplings between vibration modes and feedback of a higher number of system states provide the possibility to control plate flow-induced vibrations with a smaller actuator effort in the positions different from those obtained by the maximum controllability and the maximum stability criteria. It must be remembered that the mentioned criteria are based on the first and the second vibration modes of the system and do not account for aerodynamic couplings between these vibration modes and high-frequency ones. However, it is not recommended to use an LQR controller that contains a large number of state feedbacks. The state estimator required for such a controller implies a considerable computation cost and difficulty. Moreover, the estimation of high-frequency vibration states always is accompanied by significant errors, and finally, the external and sensor noises reflected in the high-frequency states are amplified considerably during state feedback procedure.

With the aim of investigating the effect of gaining matrices **Q** and **R** on the controller performance, the controller performance index (Eq. (39)) in two patch locations and for different values of gaining matrix components (i.e. $\bar{Q}$ and R) is calculated. The patch locations selected for this analysis match with Pos. 1 and Pos. 3 of the previous analysis. The air dynamic pressure is set to $\lambda = 290$. The obtained results are reported in Table 9. From this table, one can see that the performance index value corresponding to the Pos. 1 is always smaller. This means that the maximum controllability index defines the locations where the controllability index is minimized. However, from the previous analysis, we show that the locations obtained by this method need higher values of the voltage amplitude.

Table 9 LQR controller performance index defined for a 5 DOF model with respect to the gaining matrix components

$\bar{Q}$	0	1,000	10,000	100,000	1,000,000	1,000,0000
$R = (1/500)^2$						
J (Pos1)	0.0746	0.0747	0.0748	0.0754	0.0818	0.128
J (Pos3)	0.164	0.164	0.164	0.165	0.176	0.255
$R = (1/5,000)^2$						
J (Pos1)	7.46e−4	7.54e−4	8.18e−4	0.0013	0.0034	0.0128
J (Pos3)	0.0016	0.0017	0.0018	0.0026	0.0067	0.0246
$R = (1/50,000)^2$						
J (Pos1)	7.46e−6	1.28e−5	3.44e−5	1.27e−4	5.08e−4	0.0018
J (Pos3)	1.64e−5	2.55e−5	6.77e−5	2.45e−4	0.001	0.0048

The flow dynamic pressure is set to $\lambda = 290$

8 Conclusions

In this paper, the optimal location of a bonded piezoelectric patch for flutter stabilization of a cantilevered rectangular plate has been investigated via controllability and dynamic stability criteria. According to the controllability criterion, the best position for patch placement is a position where the controllability index is maximized. Instead, a dynamic stability criterion, developed in this paper, obtains the patch locations where the flutter boundary is enhanced passively and flow-induced vibrations can be suppressed with a small actuator effort. Results show that for cantilevered plates bonding a patch with a small mass ratio changes the critical dynamic pressure considerably. This yields a significant change in the system dynamics. A survey in the literature shows that this effect is ignored by many researchers.

Since the maximum actuation voltage is restricted by the piezo-actuator allowed voltage, this constraint must be regarded in practical controller design and patch placement strategies. In our survey, this value has been considered as a norm to assess placement approaches. For active control of induced vibrations, two control plans are utilized: feed back of flutter involved modal states (the first and the second modal states) and LQR full-state feedback. Reduced order models are used for the latter case.

Numerical results reveal that when merely the first and the second system modal states are used as control feedbacks, the best location for patch placement matches with those obtained by dynamic stability criterion, i.e., the patch locations where the maximum passive stability is obtained. This judgment is still valid when an LQR controller with low number of feedback states and a reduced model estimator are utilized. When an LQR controller with a large number of state feedbacks is employed, the best patch position is defined by maximizing the controllability index. However, utilization of such a controller will face the designer with some mathematical and practical limitations.

While the main aim of investigators is to suppress vibrations of fluttering plates, the presented results suggest that utilization of a passive–active hybrid method can present a satisfactory performance for vibration stabilization of the mentioned systems. These results suggest that there is a possibility to find actuator locations where the controllability index is not optimal; instead, the aeroelastic characteristics of the system are modified so that the needed actuator effort reduces, and therefore, the overall control performance improves considerably.

References

1. Moon, S.H., Kim, S.J.: Active and passive suppressions of nonlinear panel flutter using finite element method. AIAA J. **39** (2001)
2. Abdel-Motagaly, K., Guo, X., Duan, B., Mei, C.: Active control of nonlinear panel flutter under yawed supersonic flow. AIAA J. **43** (2005)
3. Moon, S.H.: Finite element analysis and design of control system with feedback output using piezoelectric sensor/actuator for panel flutter suppression. Finite Elem. Anal. Des. **42**, 1071–1078 (2006)
4. Han, J.H., Tani, J., Qiu, J.: Active flutter suppression of a lifting surface using piezoelectric actuation and modern control theory. J. Sound. Vib. **291**, 706–722 (2006)
5. Nam, C., Kim, Y., Weisshaar, T.A.: Optimal sizing and placement of piezo-actuators for active flutter suppression. Smart Mater. Struct. **5**, 216–224 (1996)
6. Richard, R.E., Clark, R.L.: Delta wing flutter control using spatially optimized transducers. J. Intell. Mater. Syst. Struct. **14**, 677–691 (2003)
7. von Karman, T.: Festigkeitsprobleme im Maschinenbau. Encyclopädie der Mathematischen Wissenschaften. **4**, 352–384 (1910)
8. Kane, T., Levinson, D.: Dynamics: Theory and Application. McGraw-Hill, New York (1985)
9. Sander, G., Bon, C., Geradin, M.: Finite element analysis of supersonic panel. Int. J. Numer. Methods Eng. **7**, 379–394 (1973)
10. Mei, C., Abdel-Motagaly, K., Chen, R.: Review of nonlinear panel flutter at supersonic and hypersonic speeds. Appl. Mech. Rev. **52**, 416–421 (1999)
11. Mallik, N., Ray, M.C.: Effective coefficients of piezoelectric fiber-reinforced composites. AIAA J. **41**, 704–710 (2003)
12. Sadri, A.M., Wright, J.R., Wynne, R.J.: Modelling and optimal placement of piezoelectric actuators in isotropic plates using genetic algorithms. Smart Mater. Struct. **8**, 490–498 (1999)
13. Dowell, E.H., Curtiss, H.C., Scanlan, R.H., Sisto, F.: A Modern Course in Aeroelasticity. Kluwer Academic Publishers, Dordrecht, The Netherlands (1989)